8

Muon and Neutral Hadron Detector

8.1 Physics Requirements and Performance Goals

Muon identification and neutral hadron detection are provided by the Instrumented Flux Return (IFR), which makes use of the large iron structure needed as the magnet return yoke. Excellent muon identification over the widest possible momentum range and the ability to detect K_L^0s are distinctive features of the BABAR detector.

At the $\Upsilon(4S)$, muons are produced mostly in semileptonic decays, either directly from the B mesons or from the cascade Ds. The sign of the charge determines the b or c flavor of the parent meson, thus providing a clean tag for the CP-asymmetry measurements.

For all particle species, the asymmetry of the machine results in a strong correlation between momentum and angle. The absolute population and the shape of the muon momentum spectra are quite different in the backward, central, and forward regions of the detector, as can be seen in Figure 8-1.

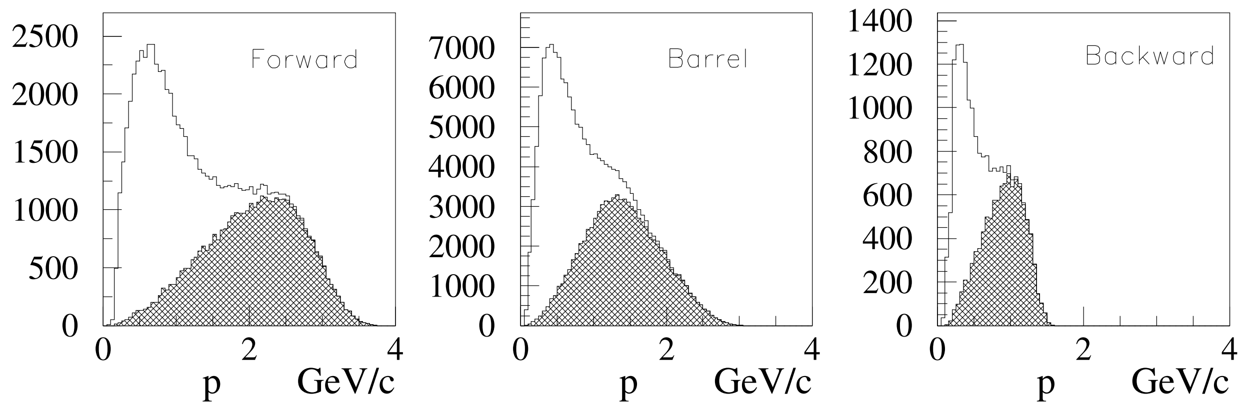

Figure 8-1. *Momentum distribution of direct and cascade muons in (a) the forward endcap, (b) the barrel, and (c) the backward endcap regions. The shaded part of the histogram refers to direct decays.*

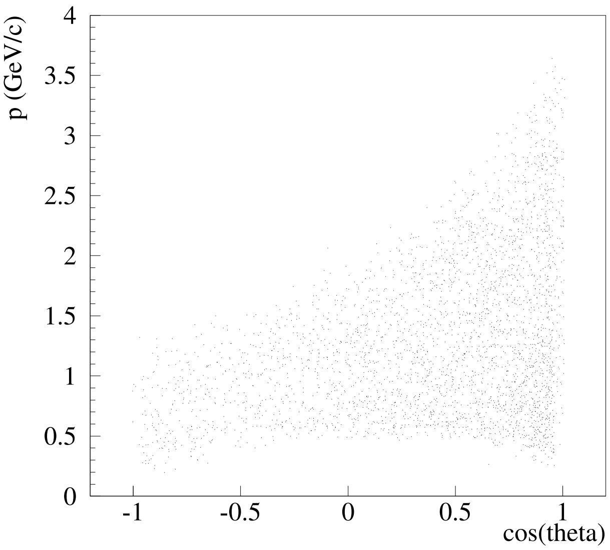

Figure 8-2. *Correlation between momentum and $\cos\theta$ for particles reaching the IFR; different momentum cut-offs for barrel and endcaps can be seen.*

The main goal for the IFR detector is to achieve the highest practical tagging efficiency. About 18% of all B decays contain at least one muon in the region covered by the *BABAR* detector; these are roughly divided into 8% with a direct muon, 8% with a cascade muon, 1% with a muon from a τ decay, and 1% dimuon events. High momentum muons ($p \geq 1.2\,\mathrm{GeV}/c$) are mostly direct decays, while muons from D decay peak at $500\,\mathrm{MeV}/c$. A gain of almost a factor of two in tagging efficiency can be achieved if one can also detect low momentum (well below $1\,\mathrm{GeV}/c$) muons and correctly assign them to B or cascade D decays. Detection of low momentum muons will also improve the measurement of $|V_{bc}|$ by reducing the systematic error in the extrapolation to low momenta.

The muon momentum range to be covered by the IFR therefore extends up to a few GeV/c; the lower end of the range is fixed by magnetic bending in the barrel region ($\sim$450 MeV/c) and by energy losses in the inner detectors ($\sim$250 MeV/c) in the two endcap regions, as shown in Figure 8-2.

Charged tracks found in the central drift chamber will be matched to tracks in the IFR. Identification as muons or hadrons will result from detailed analysis of the hit patterns in the active detectors. The ratio of muons to hadrons in the three sections of the detectors is shown in Figure 8-3. The maximum tolerable level of hadron misidentification will depend on the physics topics under study; for tagging purposes, it has been shown that the hadron contamination in the muon sample should not exceed the 15% level. This translates into an upper limit of 5% for the probability that a hadron will be identified as a muon.

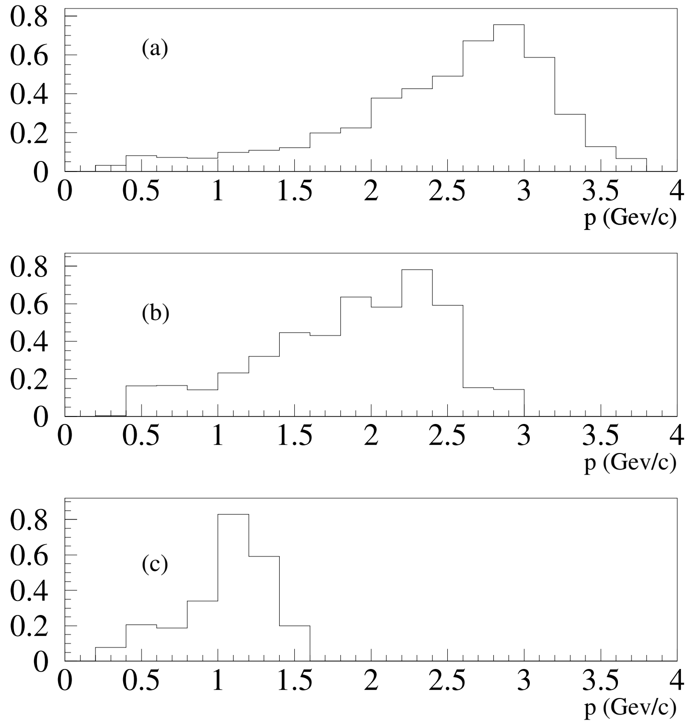

Figure 8-3. *Muon to hadron ratio as a function of momentum in the three sections of the detectors: (a) forward endcap, (b) barrel, and (c) backward endcap.*

The IFR also constitutes a hadron calorimeter; it will allow the detection of K^0_Ls and other neutral hadrons. A measurement of the K^0_L energy is not foreseen due to the limited calorimetric resolution. In any event, such a measurement produces no real improvement in event reconstruction. The hits induced by the charged secondaries produced in the K^0_L interaction will be used to detect K^0_Ls. (About 70% of K^0_Ls interact before reaching the IFR.) The K^0_L direction is then inferred from the location of the energy deposition. The ability to identify K^0_Ls and reconstruct their directions creates the opportunity to use the decay $B^0 \to J/\psi K^0_L$ for *CP*-violation studies. This could provide an event sample comparable to the benchmark decay $B^0 \to J/\psi K^0_S$ and act as a systematic check on any observed CP asymmetry, since K^0_L and K^0_S are opposite *CP* states. The parent B can be reconstructed from the four-vector of the J/ψ, measured in a leptonic decay, and the direction of the K^0_L.

The momentum spectrum for K^0_Ls produced in $B\overline{B}$ events peaks at 500 MeV/c (Figure 8-4). K^0_Ls from $B^0 \to J/\psi K^0_L$ are more energetic, as can be seen in Figure 8-5(a). Since this case is a two-body decay, the momentum distribution is practically flat, and extends from 1 to 3 GeV/c. The K^0_S detection efficiency averaged over this momentum range is ~50%; this is the benchmark with which to compare the K^0_L detection efficiency. The measurement of the K^0_L direction is enough to identify the $B^0 \to J/\psi K^0_L$ decay, given the strong correlation

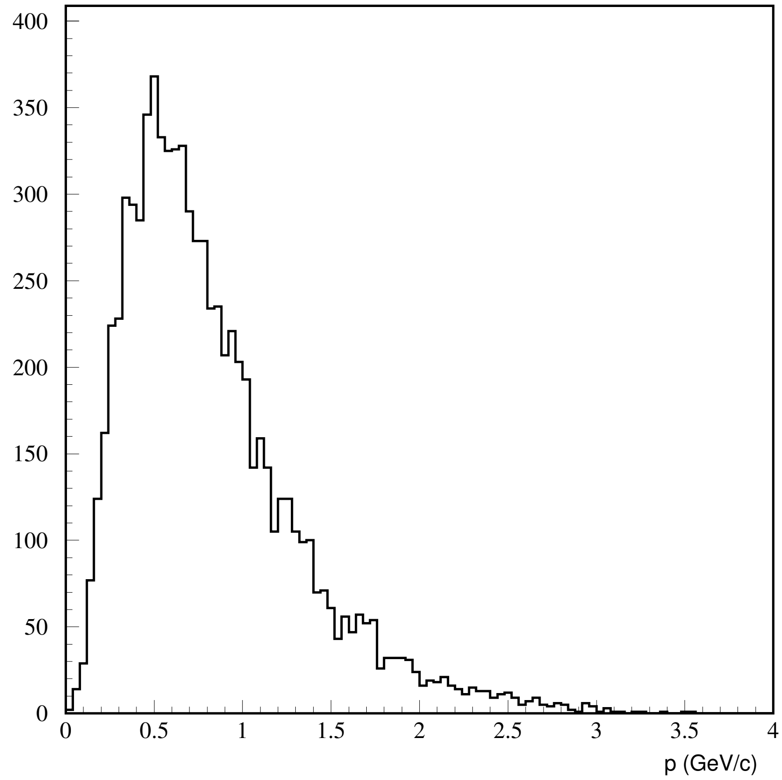

Figure 8-4. *Momentum distribution for all K_L^0s produced in $B^0\overline{B}^0$ events.*

between momentum and angle. The spread can be seen in Figure 8-5(b) and is due to the B's momentum distribution. However, a few significant physics backgrounds must also be handled. Decays of both charged and neutral B mesons to $J/\psi\, K^*(892)$, in which the $K^*(892)$ decays to a $K_L^0\pi$ pair, produce events that can directly mimic the desired signal with branching ratios slightly larger than the signal. The momentum distribution and the momentum angle correlation of the K_L^0s produced in this process are shown in Figure 8-6. These backgrounds can be suppressed by identifying the extra pion and reconstructing the $K^*(892)$ mass. Events in the charged case, $B^+ \rightarrow J/\psi\, K^{*+},\ K^{*+} \rightarrow K_L^0\pi^+$, may be further suppressed by rejecting events in which the charged pion can be associated with an isolated J/ψ vertex.

To improve the signal to background ratio, it is essential to have good resolution in the measurement of the K_L^0 direction in addition to an efficient reconstruction of the K_L^0. Figure 8-7 shows the dependence of the signal and of the background, before any other cut is applied, on the angular resolution of the detector. The K_L^0 detection efficiency improves steadily with a finer iron segmentation, as shown later in this chapter.

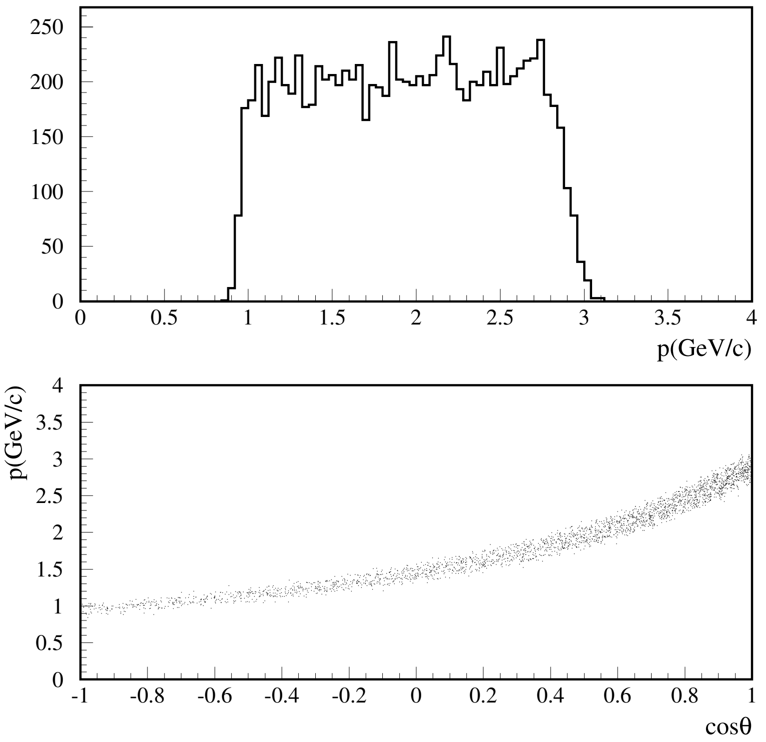

Figure 8-5. *The momentum distribution and the momentum vs. angle correlation for all K^0_Ls produced in $B^0 \to J/\psi\, K^0_L$ decays.*

K^0_L detection is useful in channels for which the K^0_L direction alone is sufficient to reconstruct the momentum of the parent B. In particular, several D decays can be fully reconstructed using charged tracks in a separate vertex and the direction of the K^0_L. For example, we have tested the possibility of reconstructing the decay $D^- \to K^0_L\pi^+\pi^-\pi^-$. Decays of B^0 to $D^-\pi^+$ have been generated in which the D^- is then allowed to decay to $K^0_L\pi^+\pi^-\pi^-$. The three-pion D^- decay should allow a good vertex reconstruction. The K^0_L is then reconstructed by measuring its direction in the IFR system and recomputing its momentum under the assumption that it comes from a D^- decay. Figure 8-8(a) shows the resulting K^0_L momentum distribution together with the fraction interacting in the IFR (shaded area). Figure 8-8(b) shows the resulting $D^-\pi^+$ effective mass for those events which can be reconstructed. Requiring in addition a recoil $\bar{B}^0$ (Figure 8-8(c)) should allow this decay mode to be detected with little background.

In addition to exclusive event reconstruction, the IFR can be used to veto events with missing hadronic energy, in particular background events for the decay $B \to \tau\nu_\tau$; when used as a veto, it is obviously essential for the detector to have as complete a solid angle coverage as practical and the highest possible efficiency.

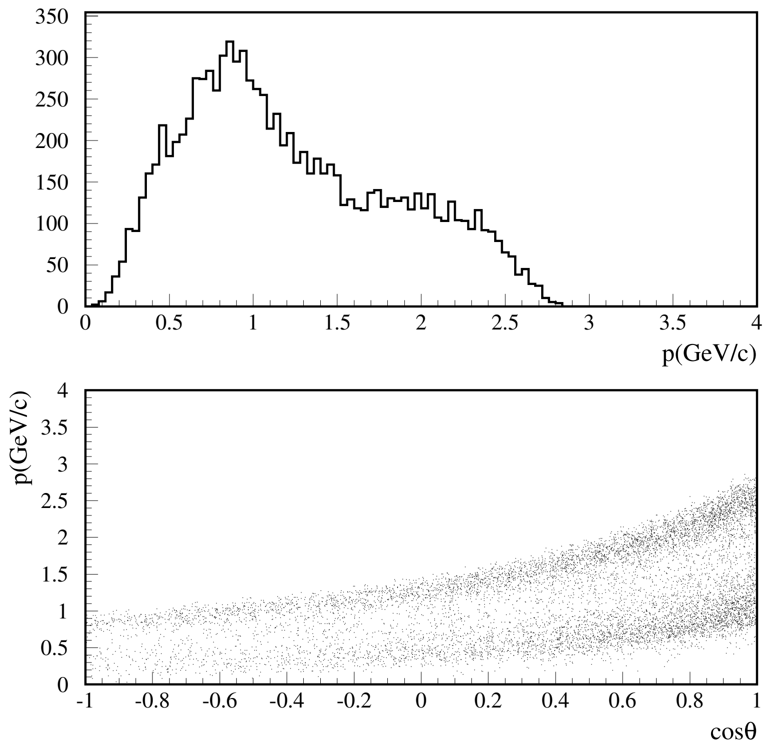

Figure 8-6. *The momentum distribution and momentum vs. angle correlation of the K_L^0s produced in $B \to J/\psi K^*(892)$.*

8.2 Detector Overview

8.2.1 The Iron Structure

The muon and neutral hadron detector uses as an absorber the flux return iron of the 1.5 T superconducting solenoid; this massive steel structure also serves as the support for the inner detectors.

The design of the iron plates has to take into account both the requirements dictated by its use as hadron absorber and muon filter and the complex mechanical problems caused by the need to provide access to the inner detectors, all subject to the space constraints imposed by the machine components and the experimental hall.

The IFR consists of three main components: the barrel and the backward and forward endcaps. The barrel extends radially from 1.78 to 3.01 m and is divided into sextants; the length of each sextant is 3.75 m, and the width varies from 1.88 to 3.23 m. Each endcap

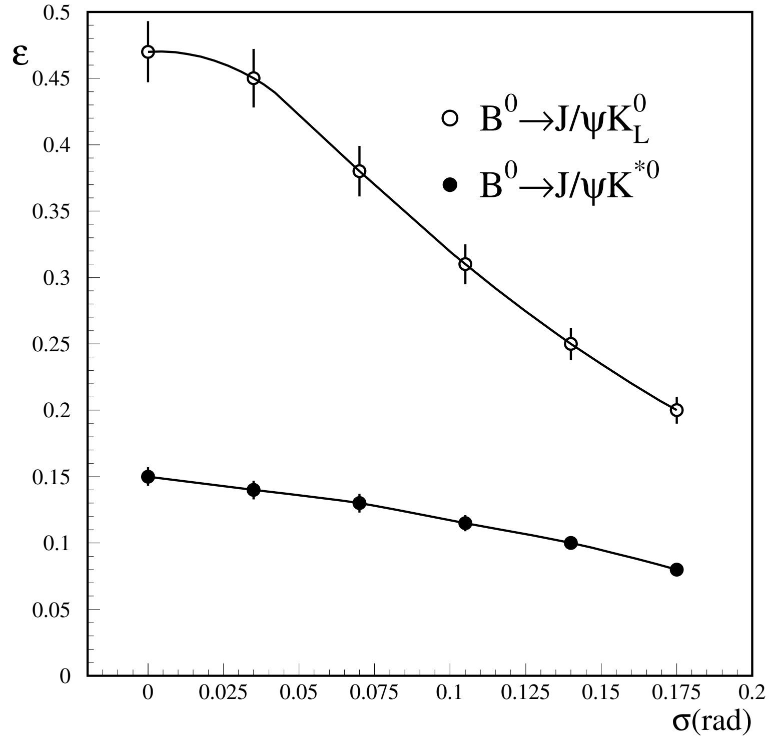

Figure 8-7. *Signal and background efficiencies for reconstructing $B^0 \rightarrow J/\psi K_L^0$ as functions of the angular resolution in the K_L^0 direction.*

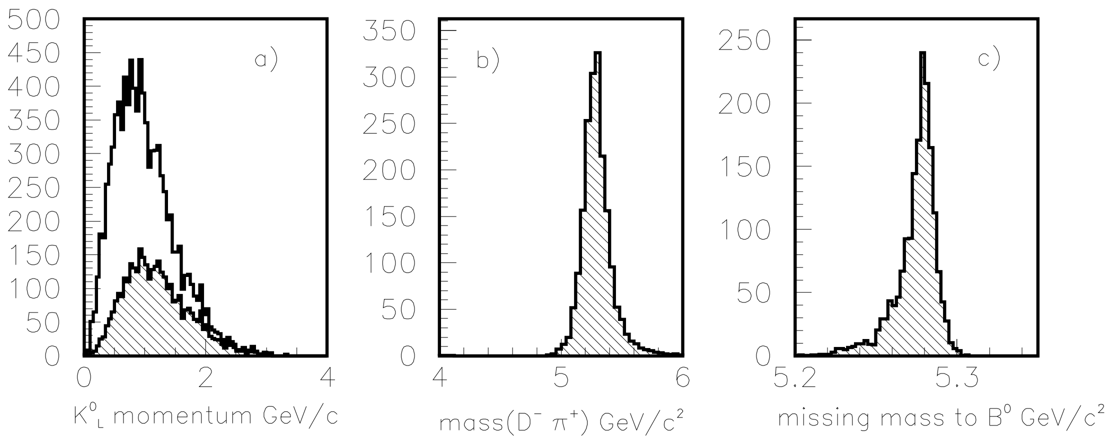

Figure 8-8. *(a) Reconstructed K_L^0 momentum from $D^- \rightarrow K_L^0\pi^+\pi^-\pi^-$. The shaded area represents the fraction interacting in the IFR. (b) $D^-\pi^+$ effective mass distribution. (c) Missing mass to the reconstructed $B^0 \rightarrow D^-\pi^+$.*

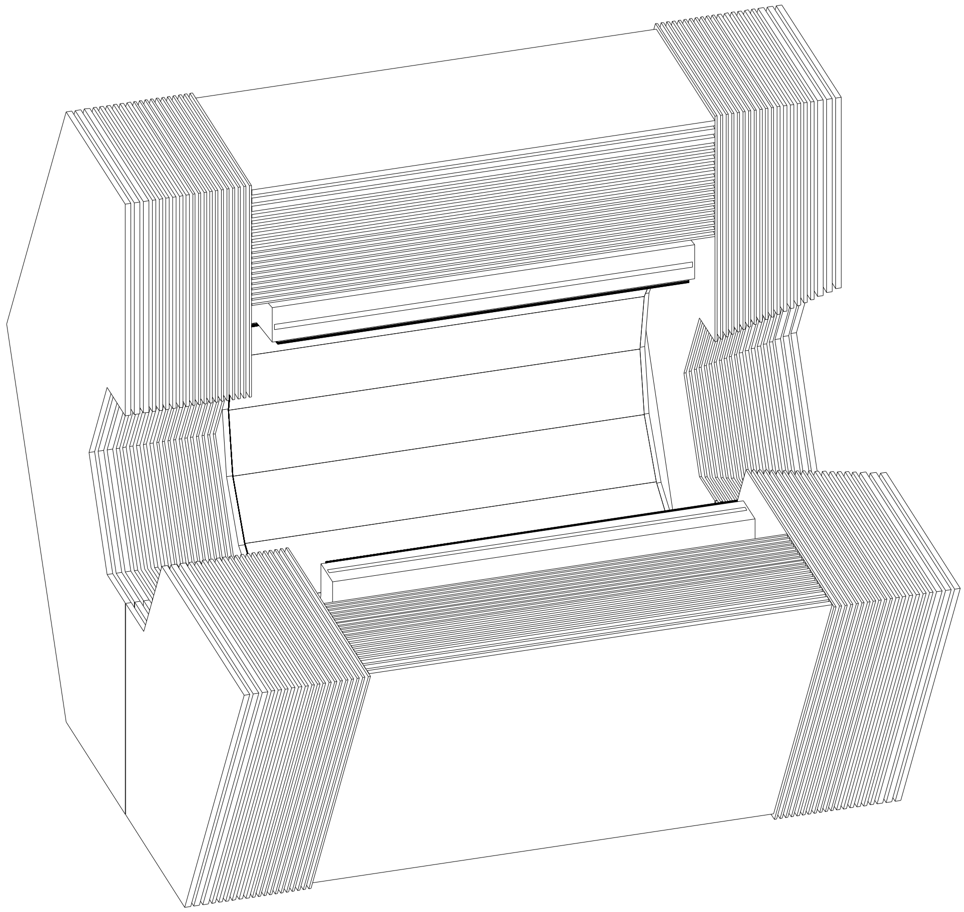

Figure 8-9. *The IFR detector.*

consists of hexagonal plates, divided vertically into two parts to allow opening of the detector and has a central hole for the beam components and the magnetic shields.

The plates are tied together by side steel plates whose thickness (5 cm) reduces the area available for the active detector. The dead area is concentrated at the joining of the hexagonal blocks and accounts for a small loss in solid angle, approximately 7%. The endcap gaps are divided into three by stiffeners needed to prevent bending due to the magnetic forces and to limit the stress due to mechanical and potential seismic loads. A view of the detector is shown in Figure 8-9.

The iron segmentation is dictated by the physics requirements of identifying low-momentum muons and detecting K_L^0s. The plate thickness is graded from 2 cm for the inner plates to 5 cm for the outer ones, based on simulation studies which will be described below. The structure consists of 11 plates 2 cm thick followed by six plates 3 cm thick and three plates

5 cm thick. The total thickness is 55 cm and is the result of a compromise between the cost, which scales with the volume, and the need to reduce hadron punchthrough. Most of the simulations, however, have been done with a total thickness of 60 cm of iron (this has been the reference design).

The fraction of B-decay hadrons reaching the IFR that will fail to be absorbed in 55 cm of iron is 1.3% overall: 0.2% in the backward region, 1.0% in the barrel, and 1.7% in the forward endcap.

8.2.2 The Active Detector Choice

The IFR detectors will cover a surface of approximately $2500\,\mathrm{m}^2$; they will be inserted in the gaps between the iron plates where access and replacement will be very difficult, perhaps impossible. It is, therefore, necessary that the technique chosen be simple and reliable as well as low in cost. Two technologies were considered, one using Plastic Streamer Tubes (PSTs) and the other using Resistive Plate Counters (RPCs). RPC technology was chosen for its superior flexibility and performance and larger active area. It was originally developed by R. Santonico and collaborators [San81, San88]; the technology is now well past its development stage, having been successfully used in several experiments [Accel, Cosmi]. A large ($\sim 600\,\mathrm{m}^2$) system is presently in use in the L3 [L3RPC] experiment at CERN, and much larger systems are now being designed for the LHC experiments [LHC94].

As will be discussed in more detail in Section 8.4.1, the proposed RPC is essentially a gas gap at atmospheric pressure enclosed between two 2 mm-thick Bakelite (phenolic polymer) plates with bulk resistivity on the order of $10^{11}\,\Omega$- cm. These electrodes are coated on their outer faces, with thin graphite layers connected to high voltage ($\sim 8\,\mathrm{kV}$) and to ground, respectively. A crossing charged particle produces a quenched spark that produces signals on external pick-up electrodes.

Active R&D is ongoing in *BaBar* and other groups to select a nonflammable and environmentally safe gas mixture.

Several RPC modules will be joined together to fill each IFR layer; on the two sides, planes of orthogonal readout strips will be attached for signal readout, so that a space point will be measured for each hit. The design of the strips is not finalized yet, pending further studies of the granularity needed. The total number of digital readout channels calculated on the basis of a 3 cm pitch is $\sim$40,000. Using data from the L3 chambers and Monte Carlo simulations we will investigate whether a coarser granularity will suffice and whether better performance can be obtained by grading the pitch with the distance from the IP. The construction of the strip planes, *i.e.,* the gluing of pre-made aluminum strips on a PVC support, is considerably faster than that of the chambers, so this item is not on the critical path. We defer final decisions until after the completion of more sophisticated Monte Carlo simulations.

Each layer will be inserted into the iron gaps as a single object using appropriate tooling; readout electronics cards will then be positioned near the gap border where they will be readily accessible for testing and maintenance; the last 20 cm of each gap will therefore be made 10 mm wider, to make room for the cards and cables.

8.3 Projected Performance

8.3.1 Muon Identification

Muons are positively identified if they penetrate all layers of the iron. Non-penetrating muons (below 1.1–1.5 GeV/c, depending on the incidence angle) can be identified from the ionization losses in the iron. Pion separation is achieved through a combination of range and hit pattern cuts; its effectiveness increases with segmentation.

Following the program outlined in the *Letter of Intent*, several simulation studies have been performed in order to determine the IFR configuration with optimal performance for cost. In order to study a large number of segmentation configurations, as a starting point we simulated, using the GEANT implementation of the BaBar detector geometry, an IFR geometry consisting of 61 detector layers 1.2 cm thick alternating with 60 plates of iron of 1 cm thickness. The ratio of iron to detector thickness was chosen to be the same as in the *Letter of Intent* geometry, in which 24 iron planes of 2.5 cm were alternated with 25 detector layers of 3 cm. Using this method, all configurations with iron thicknesses that are multiples of 1 cm can be reproduced by switching off the undesired planes at the analysis level. We have studied many possible configurations, including both uniform and graded, as a function of radial distance from the beam, thicknesses. The minimum plate thickness studied is 2 cm; plates thinner than 2 cm are not considered practical for mechanical reasons.

The BEGET generator [Wri94] is used to produce $B^0\overline{B}^0$ events in which the B^0 can decay into any channel (branching ratios from [PDG94] are used), and the $\overline{B}^0$ becomes invisible to the detector. In this way, B^0 tagging can be studied, assuming that the *CP* eigenstate decay of the $\overline{B}^0$ is completely reconstructed.

Figure 8-10 shows the distribution of the last detector layer reached as a function of momentum for muons and pions. Muons with momentum below $\sim$1.3 GeV/c stop in the IFR, and most of the pions interact in the iron.

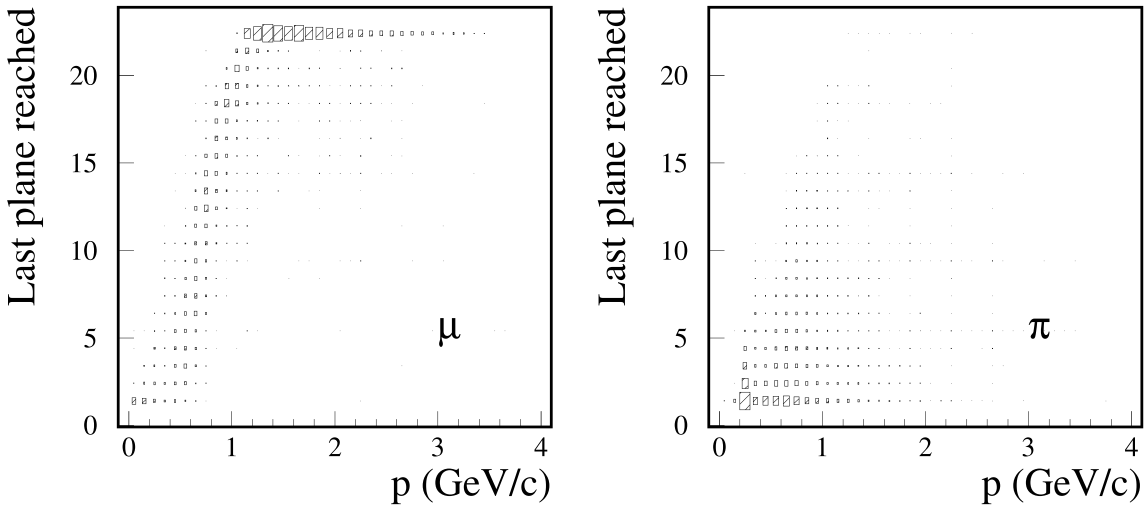

Figure 8-10. *Distribution of the last detector plane reached as a function of momentum for μ and π.*

A criterion which is particularly useful for distinguishing muons from hadrons is based on the number of planes hit versus the number of planes traversed [Calc94]. A muon track typically has one hit in each layer, while hadrons can interact strongly in the iron, generating a hadron shower with several particles producing multiple hits per layer. It is also possible that only neutrals are present, and this will cause the absence of hits in one or more planes, even for an ideal detector. In general, for pion tracks the number of planes hit is smaller than the number of planes traversed, while muon tracks have hits in almost all of the planes they traverse. The difference in the behavior of muons and pions in this respect can be seen in Figure 8-11, which shows the number of planes hit versus number of planes traversed. A cut on the difference between these numbers gives a powerful pion rejection.

In a further development of this idea [Lis94], a maximum likelihood function can be built from a detailed study of the number of hits in each plane for muons and for hadrons, as a function of momentum. This can be used to determine a combined probability for a track to be a muon or a hadron. We believe that this technique, still under development, will be the one actually used to identify muons.

Energy losses in the drift chamber and CsI calorimeter have slightly different distributions for muons and pions at low energy (Figure 8-12), and this difference can be used to reduce pion contamination at low momenta.

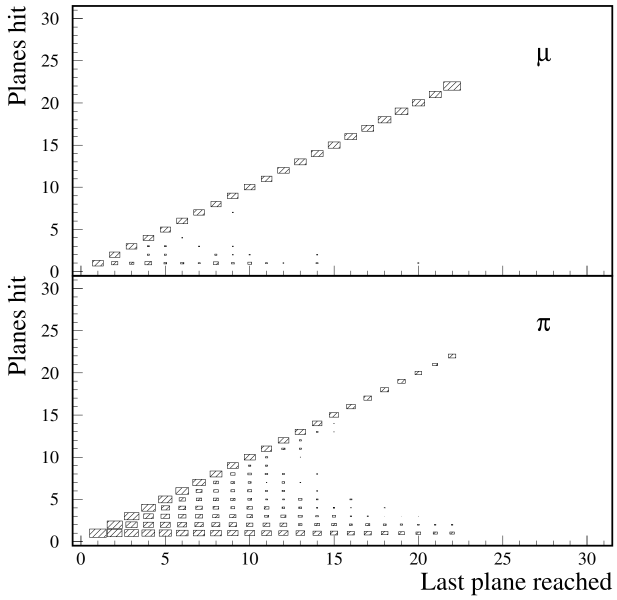

Figure 8-11. *Number of planes hit vs. number of planes spanned. The size of the boxes is proportional to the log of the number of entries. 100% detector efficiency is assumed.*

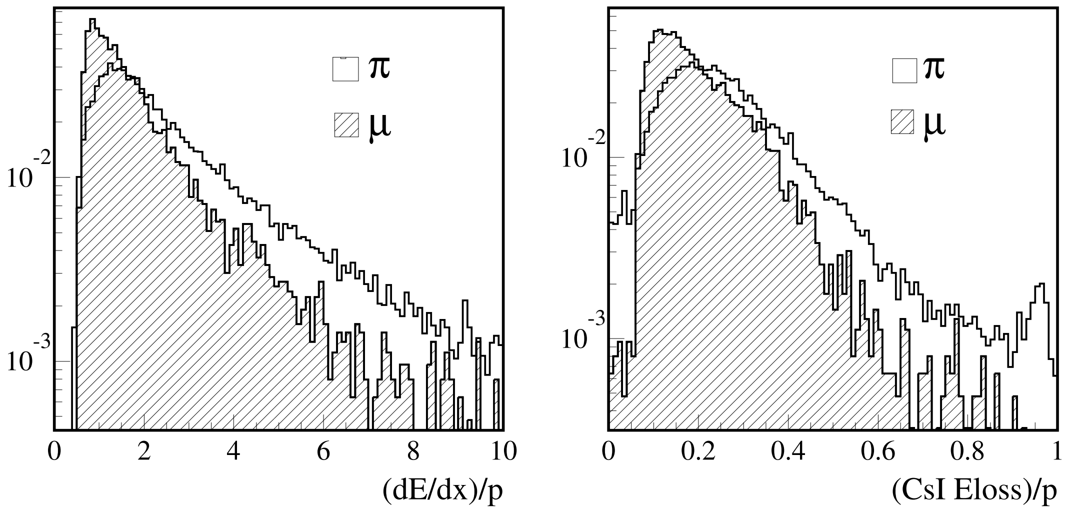

Figure 8-12. *Energy loss in the inner tracker (average per hit) and in the CsI calorimeter. Pions and muons are normalized to equal area.*

Several Monte Carlo analyses have been performed with GHEISHA and FLUKA as hadron shower generators. The variables used to discriminate muons are the following:

- Number of planes hit;
- Traversed material (Fe cm equivalent);
- Number of planes spanned versus number of planes hit;
- Number of consecutive missed planes along the track;
- Likelihood function for number of hits in each layer;
- Tracking residuals; and
- Energy deposition in the inner detectors.

Several sets of cuts depending on momentum and polar angle have been used for these variables, in order to increase efficiency while keeping hadron contamination as low as possible.

Misidentified hadrons assigned to the muon sample result in a dilution of the tagging efficiency, and introduce a background to the study of semileptonic decays and other channels containing muons. Different analyses, however, will require different tuning of these cuts. A typical example is the reconstruction of $J/\psi \rightarrow \mu^+\mu^-$ in which we can safely use loose identification criteria because of strong kinematic constraints.

Flavor tagging, on the other hand, requires a clean muon sample because the effectiveness of the tag depends strongly on the tagging purity. In this case, the background to the muon sample from misidentified hadrons can be further reduced by studying the kinematic features of the two classes of tracks [Pia94]. A set of discriminant variables, such as those shown in Figure 8-13, can be identified and a probability density function derived for each variable. From the probability distributions associated with each discriminant variable, one can calculate the probability that a track is a muon as follows [Jaf94]:

$$y^{\mu}_{eff} = 1 - \frac{\eta \prod g^{\pi}_i}{(1-\eta)\prod g^{\mu}_i + \eta \prod g^{\pi}_i}, \tag{8.1}$$

where g^{μ}_i is the probability associated with the i^{th} discriminant variable for the particle to be a muon, g^{π}_i is the similar probability for the particle to be a pion, and η is the fraction of pions in the total muon-pion sample. A simple cut in y^{μ}_{eff} has been found to correctly identify ~95% of the muons, with a rejection ratio of 15 : 1 for pions.

Configurations with uniform absorber segmentation have been studied with steel plate thicknesses ranging from 2 cm to 20 cm, and 31 to 4 detector layers, respectively. The efficiency

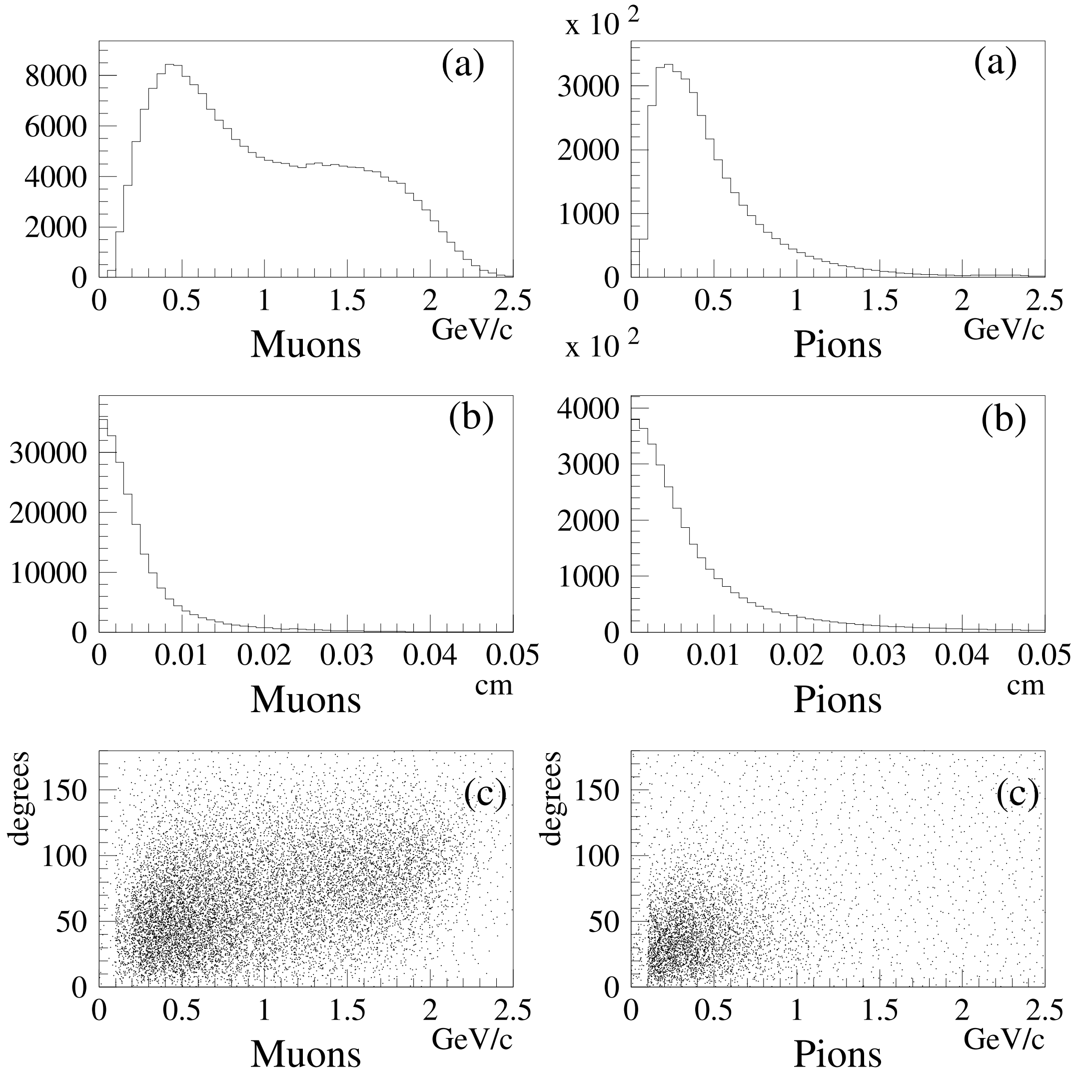

Figure 8-13. *μ/π discriminant variables: (a) center-of-mass momentum, (b) distance from the beam line, and (c) isolation, i.e., the opening angle from the closest track.*

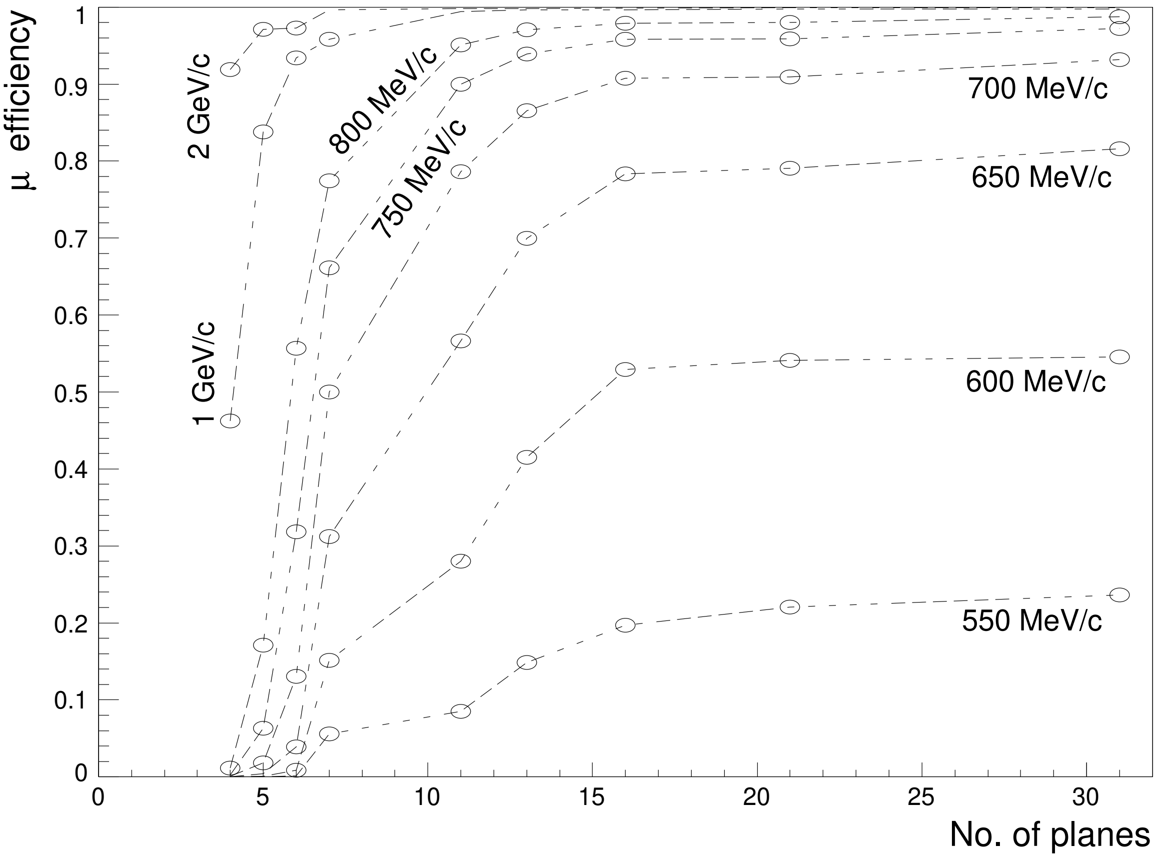

Figure 8-14. *Muon efficiency as a function of the number of detector planes for fixed momentum value. The simulation is based on FLUKA (total iron thickness of 60 cm). Passage through a detector plane is simply counted with perfect efficiency; no simulation of RPC information is incorporated. Inner detector cuts are not applied.*

for muon identification at a given hadron misidentification probability (4%) as a function of the iron segmentation is shown in Figure 8-14 for several momentum ranges.

Reducing the number of planes clearly degrades the efficiency and worsens the signal to background ratio at low momenta and, to a lesser extent, at high momenta. It is also evident from the figure that increasing the segmentation up to 30 iron plates does not improve the muon efficiency significantly for penetrating muons.

These results are obtained with a set of simplifying assumptions that detection efficiency (both geometric and for hits) is 100% and that each GEANT energy deposition gives exactly one hit in the detector. Further studies to refine this analysis are underway; it is, however, safe to assume that for a realistic detector, we will have to rely more on likelihood methods than on imposing cuts in the hit pattern. The loss in performance for configurations with a smaller number of detector planes will therefore be significant.

8.3.2 Muon Tagging

The muon identification efficiency and pion contamination obtained in these full Monte Carlo studies have been parameterized and used in an ASLUND analysis to determine the effective tagging efficiency as a function of the detector segmentation. The effective efficiency is obtained after false tags have been taken into account. False tags may arise from:

- Muons mislabeled as direct or cascade (100% wrong tag);
- Muons coming from a source other than B or D decay ($\sim$50% wrong tag); and
- Hadrons misidentified as pions ($\sim$50% wrong tag).

A sample of 1.2×10^6 Monte Carlo B decays was generated in order to study the characteristics of the direct *vs.* cascade muons and to choose discriminant variables. The kinematic method used to distinguish muons from pions was applied to distinguish direct from cascade muons. The variables found to provide the highest discriminant power were identified as the center-of-mass momentum, the recoiling invariant mass, and the isolation; their distributions are shown in Figure 8-15 for both classes of muons. The probabilities that a track belongs to either class of muons can be expressed as:

$$y_{eff}^{direct} = 1 - \frac{\eta^{cascade} \prod g_i^{cascade}}{(1-\eta^{cascade}) \prod g_i^{direct} + \eta^{cascade} \prod g_i^{cascade}}, \tag{8.2}$$

$$y_{eff}^{cascade} = 1 - \frac{\eta^{direct} \prod g_i^{direct}}{(1-\eta^{direct}) \prod g_i^{cascade} + \eta^{direct} \prod g_i^{direct}}, \tag{8.3}$$

where the g_i are the probabilities associated with the i^{th} discriminant variable belonging to either class, and η^{direct} and $\eta^{cascade}$ are the fractions of direct and cascade muons, respectively, in the total muon sample. A simple cut in the y_{eff} variables has been found to be very effective for assigning muons to the correct class.

The effective tagging efficiency reaches almost 9% for a configuration with uniform 2 cm segmentation and decreases as the steel plate thickness increases; using the graded 20-plane configuration that we propose, the figure is 8.7%; while for a 16-plane configuration, the efficiency drops below 8%.

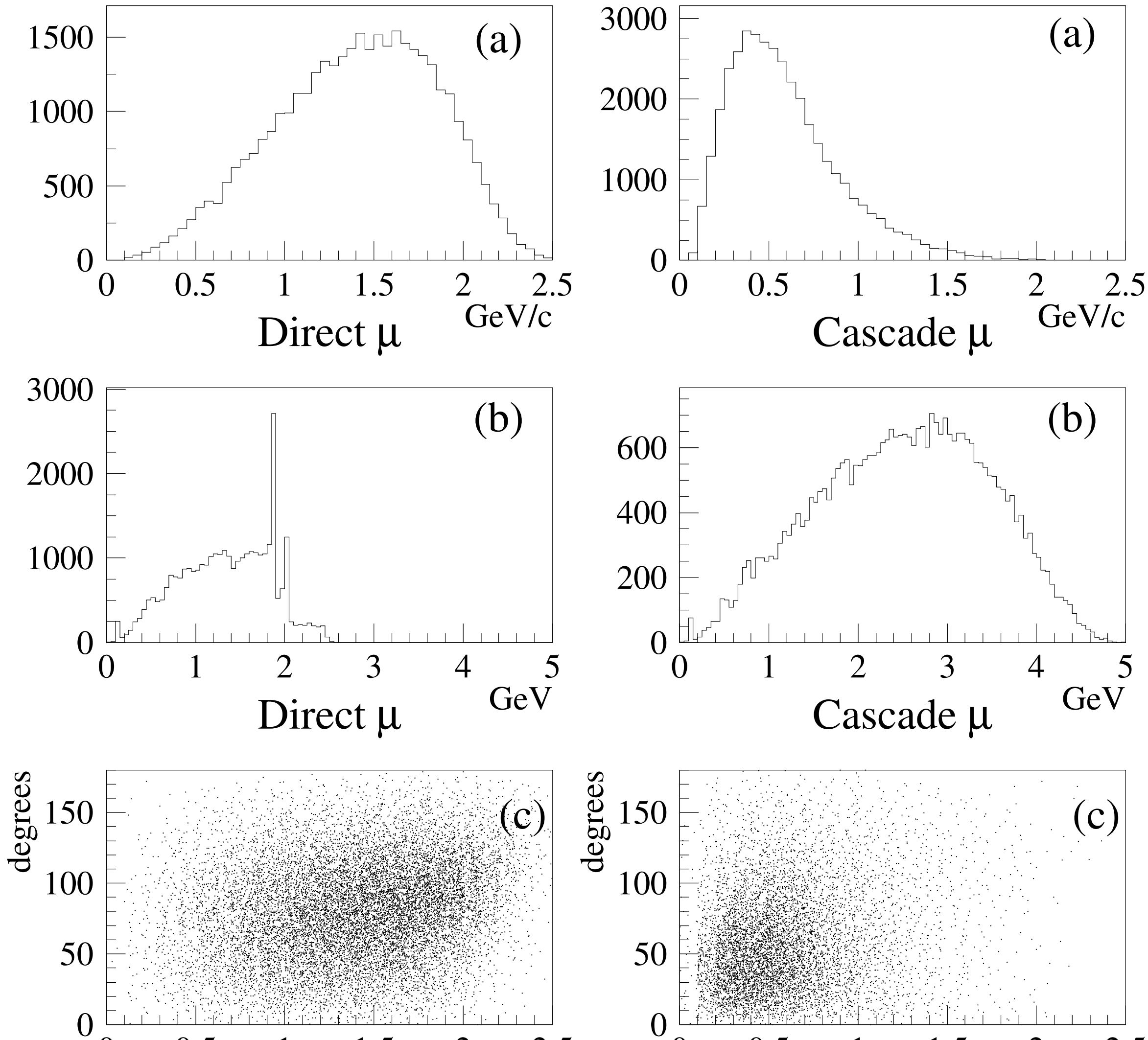

Figure 8-15. *Direct and cascade μ discriminant variables: (a) center of mass momentum, (b) recoiling invariant mass, and (c) isolation, i.e., the opening angle from the closest track.*

8.3.3 K_L^0 Detection

The two main issues for reconstructing the decay $B^0 \rightarrow J/\psi K_L^0$ are the identification of IFR hits belonging to the K_L^0 and the determination of the K_L^0 direction from those hits. Since the K_L^0s are detected via the charged secondaries from their interaction or decay, a full Monte Carlo simulation that includes hadronic interactions is required to produce a realistic hit pattern. The detector response has been simulated with BBSIM. The FLUKA hadronic simulation package has been used because the K_L^0 cross sections below 1 GeV/c in GHEISHA do not agree with the experimental data [Say68]. Full detection efficiency in both barrel and endcaps was assumed, and hit coordinates were generated assuming a 3 cm readout pitch.

A study of the effect of iron segmentation on the detection efficiency has been performed by generating single particle K_L^0 events [Bal94]. Figure 8-16 shows results for the K_L^0 detection efficiency as a function of momentum for four different configurations of iron plate thicknesses. Here, the K_L^0 signature is taken to be at least four IFR plane hits. Detection efficiency for K_L^0s improves with segmentation; thin plates are required, especially in the inner part of the detector, where most K_L^0s start or continue to interact. However, too coarse a segmentation in the outer part of the detector also decreases the efficiency for K_L^0s that start interacting in the IFR, for which the angular resolution is much better. Figure 8-16 shows that one can obtain a sizeable improvement in the efficiency by adopting a nonuniform iron segmentation; a 21-layer nonuniform configuration has much better performance than a 20-layer uniform segmentation and is almost as good as a 30-layer one.

A study of the K_L^0 identification from the IFR hits, employing pattern recognition, has been made [Wri94b]. A sample of $B\bar{B}$ events, in which one B decays to $J/\psi K_L^0$ and the other to any mode, has been generated. The K_L^0 identification process consists of clustering the hits and eliminating clusters that are near the extrapolation of charged tracks from the central drift chamber. The remaining clusters are due mostly to neutral particles (K_L^0s, neutrons, and photons from π^0s) and charged hadrons. The composition of the clustered hits in the IFR is given in Table 8-1. About 80% of K_L^0s have at least one hit in the IFR. Requiring four or more hits reduces the fraction to 68%. Neutral clusters that happen to be near a charged track are sometimes eliminated. Currently, the best algorithm reduces the K_L^0 efficiency from 68% to 56% due to these accidental overlaps.

While there is a correlation between the number of detected IFR hits and the momentum of the K_L^0 (Figure 8-18), the distribution is quite wide and depends on whether the K_L^0 interacted before reaching the IFR. This K_L^0 momentum measurement is too crude to be suitable for reconstructing and cutting on the B invariant mass.

The effectiveness of background rejection cuts depends on the angular resolution of the measured K_L^0 direction. For the K_L^0s that interact or decay before reaching the IFR, which make up $\sim$70% of the sample, the angular resolution is worsened, since the detectable

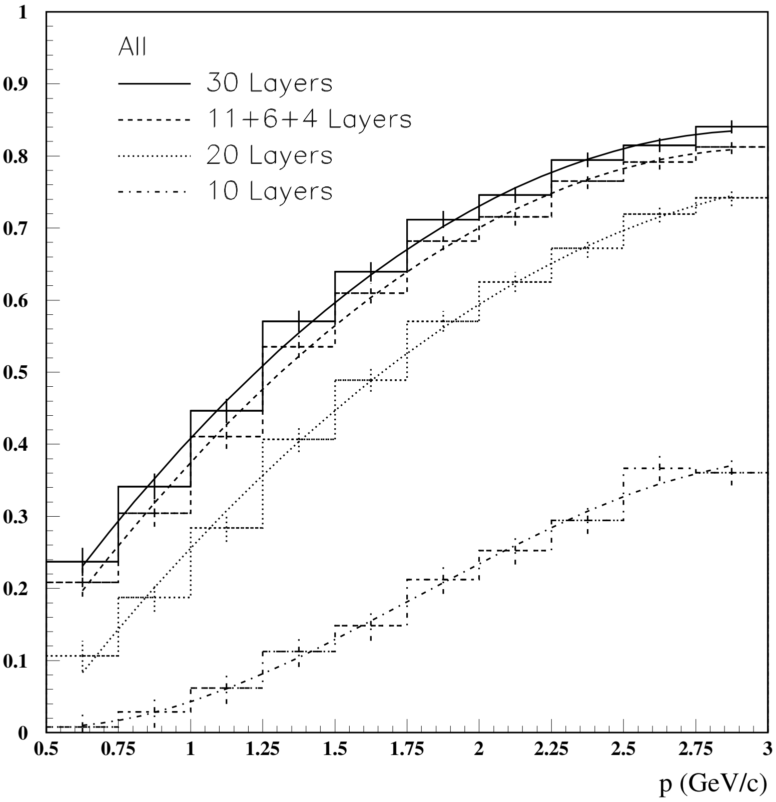

Figure 8-16. *Efficiency for detecting K_L^0s as a function of momentum. The different sets of points represent different segmentations of the flux return iron. A solution with 21 active planes with graded separation is compared.*

		Sample Composition			
		CP	Other	Other	
Criteria	K_L^0 eff.	K_L^0	K_L^0	Neutral	Charged
> 3 IFR Hits	68%	21%	4%	9%	66%
After Cuts	56%	77%	11%	4%	8%

Table 8-1. *Composition of $B^0 \to J/\psi K_L^0$ events after pattern recognition. The second line indicates the composition after a cut that removes clusters near charged tracks.*

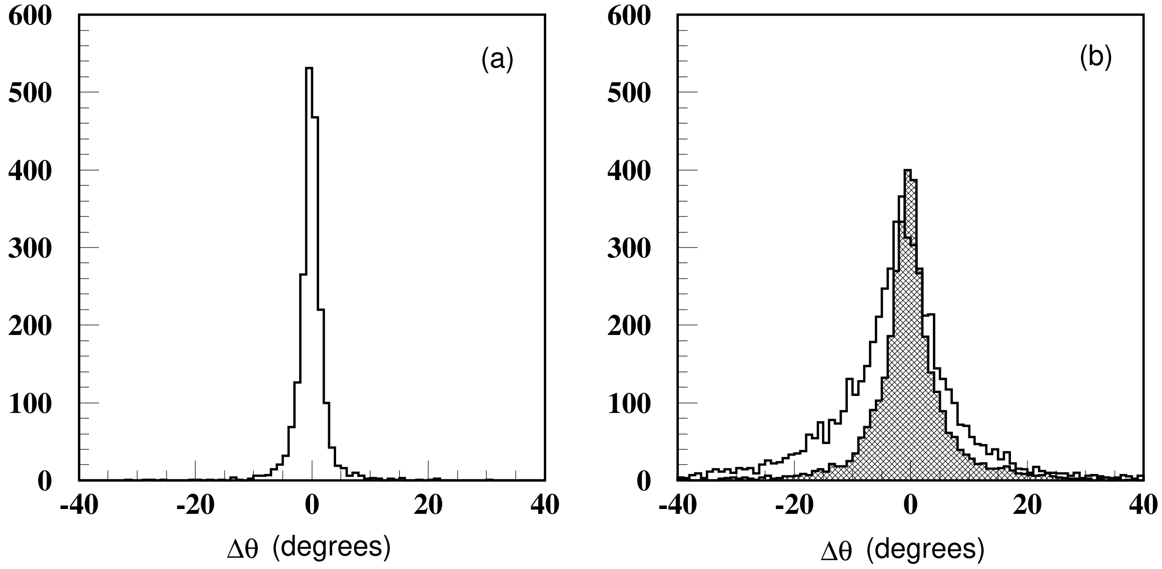

Figure 8-17. *(a) Angular resolution for K_L^0 from $B^0 \to J/\psi\, K_L^0$ determined by averaging the unsmeared IFR hit positions of K_L^0s that do not interact until reaching the IFR. (b) Angular resolution with (black) and without (open) the inclusion of a detector layer inside the coil for the K_L^0s that interacted before the IFR.*

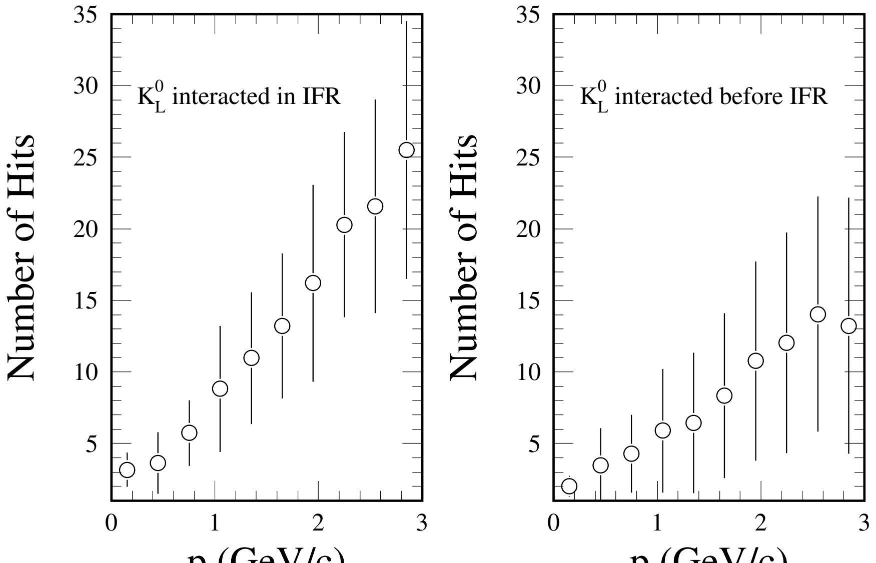

Figure 8-18. *Average number of IFR hits as a function of momentum for K_L^0 in simulated $\Upsilon(4S) \to (B^0 \to J/\psi\, K_L^0)(\overline{B}^0 \to X)$ events. The error bars represent one standard deviation of the spread in the data.*

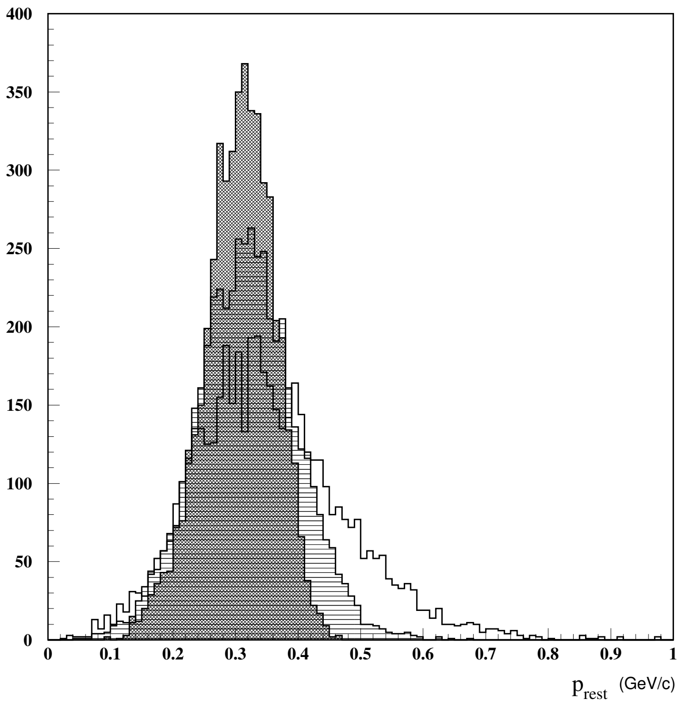

Figure 8-19. *Reconstructed momentum of the B meson in the $\Upsilon(4S)$ rest frame ($p_{\rm rest}$) for $B^0 \to J/\psi\, K^0_L$. The narrower distribution includes only the smearing effects due to the beam energy spread and finite momentum resolution. The other two histograms show the widening due to the K^0_L angular resolution for the cases in which a detector layer inside the coil is included (dashed) or not (open).*

secondaries must travel an appreciable distance and pass through additional material before reaching an active IFR detector. For example, the angular resolution for K^0_Ls that interact before reaching the IFR is about a factor of 2 worse than for those that do not interact before reaching the IFR, as shown in Figure 8-17. However, the inclusion of a detector layer inside the coil significantly reduces this smearing effect, as shown in Figure 8-17(b). Therefore, such a detector has been included in our baseline design.

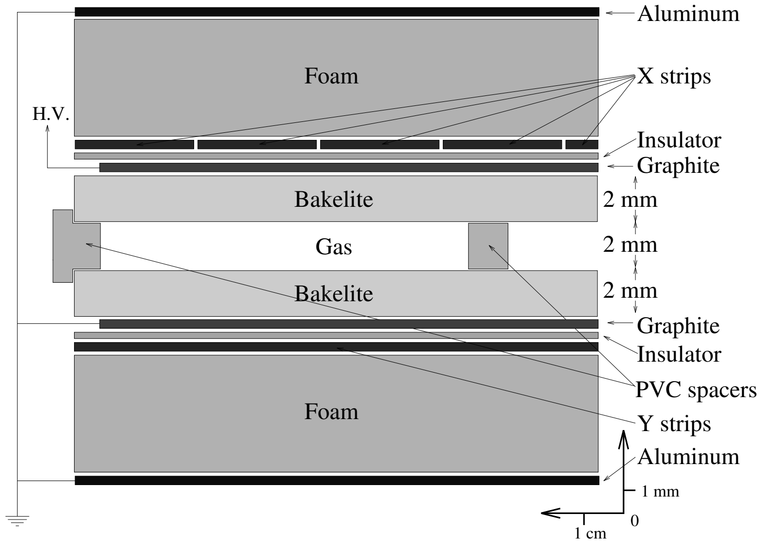

Figure 8-20. *Schematic representation of RPC components.*

8.4 Detector Design and R&D

8.4.1 Chamber Construction and Assembly

RPCs, shown schematically in Figure 8-20, have been chosen on the basis of their high intrinsic and geometrical efficiency, low cost, robustness, and flexibility in segmentation. We are planning to use the technology [San81, San88] developed by R. Santonico *et al.,* which is well-proven in various experiments, accelerators [Accel], and for cosmic ray physics [Cosmi], and whose use is foreseen in the first-level muon trigger systems designed for LHC experiments at CERN [LHC94]. The knowledge gained in years of R&D has already been transferred to industry, and the production capabilities are now well-matched to the large detector area required by *BaBar*.

As shown in Figure 8-20, the electrode plates are made of 2 mm-thick Bakelite (phenolic polymer) with a volume resistivity of 10^{11}–$10^{12}\,\Omega$-cm, painted on the external surfaces with graphite of high surface resistivity ($\sim$100 kΩ/square) and covered by two 300 μm PVC insulating films. The two graphite layers are connected to high voltage ($\sim$8 kV) and ground, respectively. Gap surfaces are treated with linseed oil, which strongly enhances RPC performance (low noise, high efficiency). Planarity of the two electrodes is assured by PVC spacers (0.8 cm^2) located on a 10 cm-square grid in the sensitive volume. The active volume is filled with an argon-based gas mixture at atmospheric pressure.

A charged particle crossing the chamber produces a quenched spark which produces signals on external pickup electrodes. There is active R&D in *BaBar* and in other groups to select a nonflammable and environmentally safe gas mixture. The discharge generated by an ionizing particle is quenched by:

- UV photon absorption by hydrocarbon molecules;
- Capture of outer electrons by electronegative additives, reducing the size of the discharge; and
- Switching off the electric field around the discharge point.

  In fact, the duration of the discharge is on the order of 10 ns, while the relaxation time of the resistive electrodes is $t = \rho\varepsilon \simeq 10^{-2}$ s, so during the discharge the electrode plates behave like insulators, and a small area around the impact point shows a deadtime on the order of t.

Induced pulses are collected on two pickup planes, 29 mm wide and separated by 2 mm, made of aluminum strips glued onto plastic foils located on either side of the chamber. Strips run in two orthogonal directions to provide two-dimensional information. The induced charge is on the order of 100 pC, and the pulse has a rise time of 2 ns and a duration of 10 ns. The low event rate in the IFR, the small size ($\sim$3 mm^2), and the short deadtime ($\sim$10 ms) of the area affected by each quenched spark mean that there is no efficiency problem. Stochastic noise depends on Bakelite plate resistivity and on the operating voltage; a value well below 1 kHz/m^2 can easily be reached.

In the upper part of Figure 8-21, the signal rate is shown as a function of high voltage for a standard mixture (Ar 59%, Isobutane 38%, Freon 13B1 3%), and with Freon 14 (CF_4) instead of Freon 13B1. The Bakelite bulk resistivity is 10^{11} $\Omega-$ cm in this test, and a clean cosmic ray plateau with negligible background can be seen with Freon 13B1. In the case of Freon 14, the plateau starts $\sim$300 V earlier, but the single rate goes up with high voltage. In any case, the singles rate is not a problem for the IFR. Assuming, for example, a singles rate of 1 kHz/ m^{2}due only to noise, we would have three random hits in a 1 μs time window around the event time for the full $\sim$2500 m^{2}IFR. If the fast timing capability of the RPC is used, by means of TDC measurements, a factor of 100 reduction can be achieved.

The efficiency plateaus for the two gas mixtures cited above are shown in the lower part of Figure 8-21. With the standard mixture, a timing resolution of $\sigma \simeq 1$ ns is reached. As reported in Section 8.5, work is presently under way at LLNL and Naples to optimize RPC performance, with the goal of using nonflammable and environmentally acceptable gases.

Taking into account the dead areas of frames and spacers, the RPC efficiency has been measured to be higher than 96%; this value can be brought closer to 100% if, for some

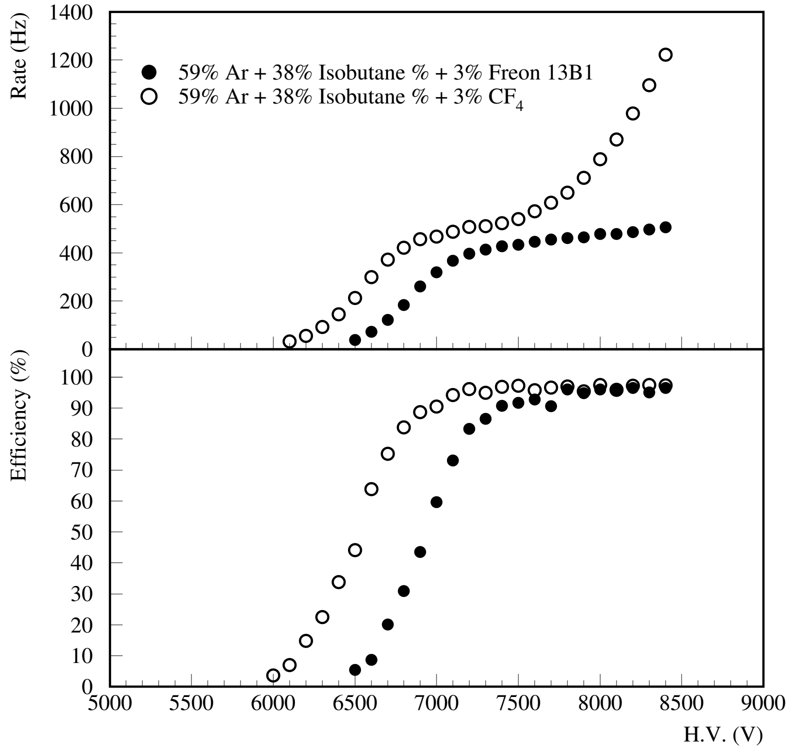

Figure 8-21. *Singles counting rate (cosmic rays and random noise) and efficiency plateaus for the two gas mixtures 59% Ar, 38% Isobutane, and either 3% Freon 13B1 or 3% CF_4.*

detector layer, a two-gap approach is chosen, as has been done in the L3 [L3RPC] experiment at LEP, with the two spacer grids staggered by 5 cm.

8.4.2 System Layout

The production plant [Plant] that we plan to use, following the excellent experience with the L3 RPCs, has developed construction tooling which allows a maximum chamber size of 1 m by 2.2 m. Within these limits, modules can be built in practically any shape. Although it is possible to modify the tooling in order to increase the maximum width and/or length, we have studied a layout of the chambers in the gaps within the present constraints. We will carefully consider the cost effectiveness of decreasing the number of modules versus retooling. Most of the cost will be based on the number of modules built, not on the total surface covered; on the other hand, major modifications to the present tooling will increase the unit cost of the chambers.

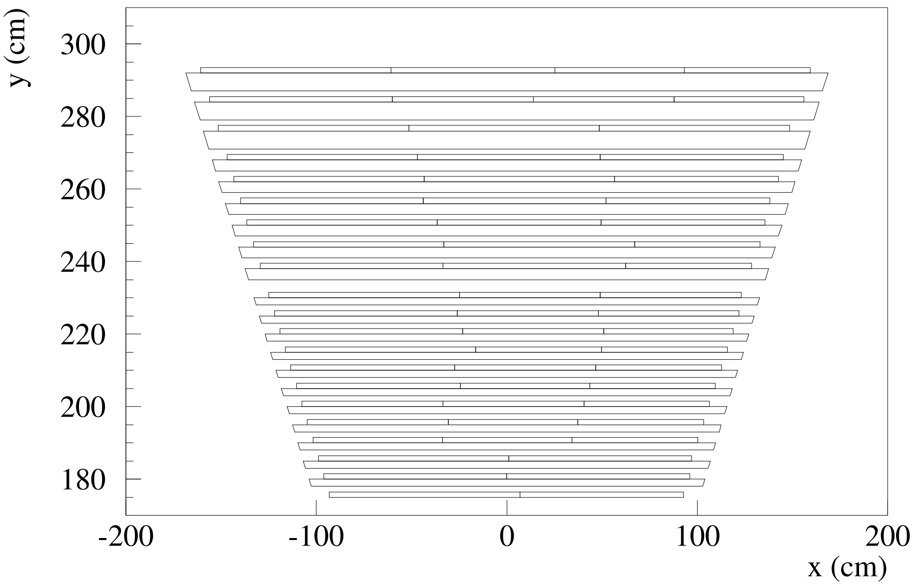

Figure 8-22. *Detailed layout of a barrel sextant. The angular coverage is in excess of 98% and is obtained with chambers of only five different widths. The extra space at each side will be used by steel plates that will hold the iron together.*

Barrel

In the six barrel sections, all the layers have the same length. The iron plates are 375 cm long, so all modules are 185 cm long and are joined in pairs; 2.5 cm is left at each end to allow for connectors, cables, and gas piping. The width of the iron gaps varies from 188 cm for the innermost layer to 323 cm for the outermost. The width of the modules therefore varies in order to ensure maximum geometric coverage. If the maximum width of each module is fixed at the 100 cm that the present production facility allows, it is necessary to use two adjacent modules in the inner layers and four in the outer ones. The total number of modules in each gap is therefore four (Layers 1 to 3), six (Layers 4 to 19), or eight (Layers 20 to 21), given the split in the z direction.

For each of the six barrel sections, 124 modules are needed, for a total of 744. Given such a large number of modules, it is important to find a layout which uses a minimum number of different sizes. This will translate into a cost and time saving not only in the production process but also in the subsequent steps. All of the quality control, testing, and assembly procedures will be greatly simplified if only a few basic shapes are needed. On the other hand, it is important to maximize the geometric coverage; as much as possible of the gap surface in each layer has to be covered.

Layer #	Radius (cm)	Gap width	Chan. 1 (cm)	Chan. 2 (cm)	Chan. 3 (cm)	Chan. 4 (cm)	Total Width
1	175	188.4	100	86			186
2	198	194.1	96	96			192
3	203	199.9	100	96			196
4	208	205.7	68	68	66		202
5	213	211.5	74	68	66		208
6	218	217.2	74	74	66		214
7	223	223.0	86	68	66		220
8	228	228.0	86	74	66		226
9	233	234.6	100	66	66		232
10	238	240.3	96	74	68		238
11	243	246.1	96	74	74		244
12	248	251.9	100	74	74		248
13	256	254.0	100	86	66		252
14	262	260.9	96	96	66		258
15	268	275.0	100	86	86		272
16	274	281.9	100	96	86		278
17	280	288.8	96	100	86		286
18	286	295.8	100	96	96		292
19	294	305.0	100	100	100		300
20	302	314.2	96	74	74	68	312
21	310	316.3	96	86	66	66	314

Table 8-2. *Active module dimensions for barrel coverage.*

For this optimization, we have relied on a computer calculation in which the gap widths are introduced with the constraints that each should be filled at least to the 98% level with 2 cm free in order to allow some clearance for the installation. With these criteria and a maximum module width of 100 cm, solutions are found starting with a minimum of six different sizes. One of these solutions is shown in Figure 8-22, and the relevant parameters listed in Table 8-2. In this layout, there are 744 barrel RPC modules in six different widths (Table 8-3).

The iron is segmented into 20 planes of graded thickness, from 2 to 5 cm as discussed in the previous subsections; the total iron thickness is 55 cm, and air gap between plates is 3 cm. Each barrel section is split into two parts to keep the weight within the crane capability available in the IR. Taking into account mechanical tolerances for joining the the two parts, the total IFR thickness is 120 cm. The total RPC area in the barrel is 1320 m^2. In each layer, four, six, or eight modules are joined, and the strip planes glued on before insertion in

Width (cm)	Number of Modules
100	144
96	156
86	108
74	132
68	72
66	132
Number of RPCs:	744

Table 8-3. *Number of different modules needed for barrel coverage.*

the iron; if the strip pitch is 3 cm, there will be a total of approximately 12,000 longitudinal and 16,000 transverse strips.

Endcaps

The endcap geometry presents a bigger challenge for defining an optimum RPC module layout, since the chambers have irregular shapes, and the presence of stiffeners between plates imposes severe constraints on chamber size and shape. The plates all have the same dimensions apart from the hole around the beam line, which differs for each of the forward endcap gaps.

Each endcap is divided vertically into halves to allow access to the inner detector without interfering with the machine components; Figure 8-23 shows the typical layout of a half layer: the maximum width and length of the modules are 100 and 220 cm, respectively, as for the barrel layout. This scheme assumes that two horizontal stiffeners 5 cm thick are sufficient to withstand the magnetic forces of a field up to 1.5 T, as discussed in Chapter 9.

All the backward endcap plates are of the same size; the inner plates of the forward endcap have a slightly smaller hole. The position of the horizontal stiffeners is the same for all plates, at 95 cm above and below the beam line, so that the layout of the chambers is the same for all plates. A few specially shaped modules of slightly different sizes have to be used in the innermost layers of the forward endcap to obtain maximum coverage.

The total number of endcap chambers is 720: 160 will be rectangular, 95 cm by 180 cm sides; 160 smaller trapezoids, 320 larger trapezoids, 80 special shapes, in three sizes. The area of plate is approximately 27 m^2, for a total of 1100 m^2 for the total RPC area required for the two endcaps.

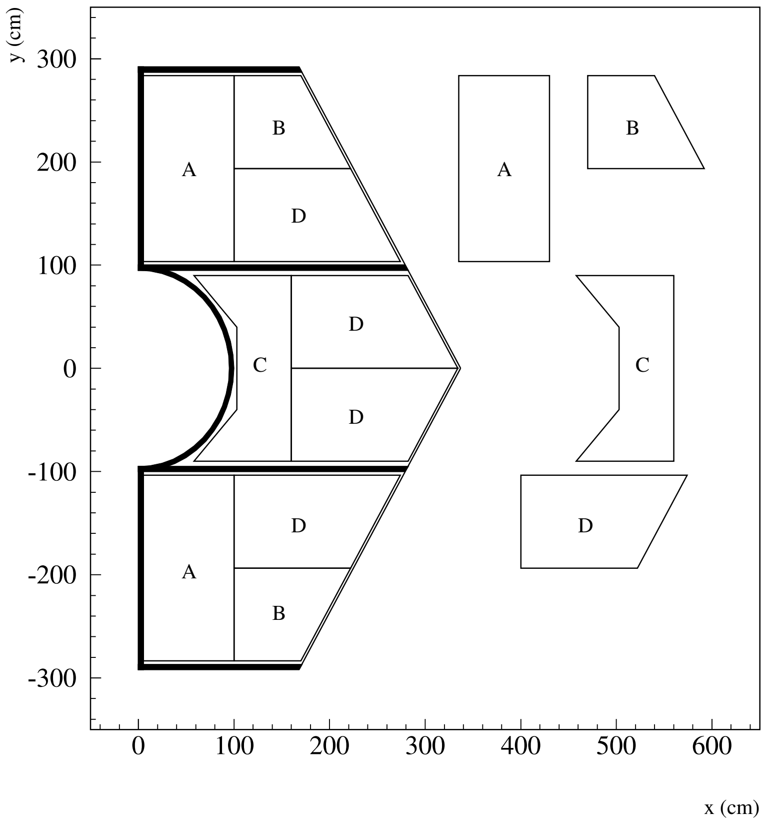

Figure 8-23. *Layout of the RPC modules in the endcaps.*

Inner Cylindrical Layer

A double-gap, resistive-plastic RPC, as shown in Figure 8-24, will be used to accommodate the largest number of coordinate planes in the 3 cm alloted space inside the solenoid. Each double-gap RPC has a single high-voltage plane made of aluminum foil laminated between two pieces of resistive plastic. The ground planes on either side of each high voltage plane have the readout strips attached to their back sides. The resulting four readout planes encode z, ϕ, u, and v coordinates with 2 cm resolution. The thickness of the entire sandwich is 2.5 cm, leaving 0.5 cm of insertion tolerance.

The inner RPC layers will be laminated together on a cylindrical mold of the final radius. The final laminate will be self supporting in its cylindrical shape. The bottom of the cylinder along the beam axis will have an open slit to accommodate the rail that supports the inner detectors. Inner RPC strips that intersect this opening (z, u, and v strips) will be brought out to the ends of the cylinder on ribbon cable. The inner RPC front-end electronics are located on the end of the cylinder.

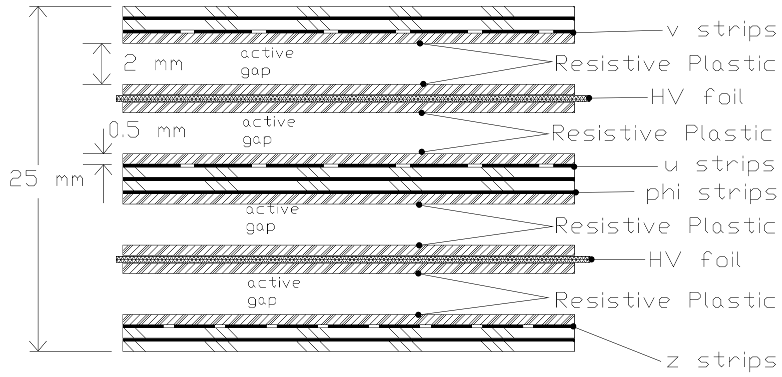

Figure 8-24. *Inner cylindrical RPC design.*

Although double gap RPCs have been successfully operated, cylindrical RPCs have never been constructed. Therefore, we will perform limited R&D on the cylindrical RPC prior to construction. This R&D will involve constructing and operating a small planar version of the inner RPC multi-gap configuration, followed by the construction and operation of a partial segment of the cylindrical inner RPC.

8.5 Gas System

8.5.1 Gas Composition and Flow Rates

The traditional RPC gas mix of 59% argon, 37% isobutane, and 4% Freon 13B1 is undesirable in two respects. Isobutane is flammable and Freon 13B1, an ozone-destroying substance, may prove difficult to obtain over the lifetime of *BaBar*. We are currently performing R&D at LLNL and Naples on nonflammable RPC gas mixes that use quenching agents besides F13B1. Both sites have precision gas mixers to prepare candidate mixtures that are fed to multiple RPCs, which are tested for efficiency, noise, cluster size, and time resolution with cosmic ray triggers. Preliminary results are encouraging. We have obtained efficient RPC operation with a mixture of 37% isobutane and no freon. We have also demonstrated efficient RPC operation using much smaller concentrations of isobutane (less than 8%) with F13B1. Preliminary tests show that the environmentally acceptable Freons 116 and 23, as well as SF6, have promising quenching properties. More evaluation of these and other gases is planned. Therefore, we plan to run the IFR RPCs with less than 10% isobutane and with 4–10% of the benign Freons 116, 23, 14, and SF6. The exact proportions of these gases must be experimentally determined to provide the highest efficiencies and maximal position resolution, at the possible expense of time resolution. Typical steady state operation of the IFR will require about two volume changes of gas per week, corresponding to a flow rate of ∼2 l/min, while startup operations are expected to require about one volume change per day corresponding to a flow rate of ∼6 l/min.

8.5.2 Mixer

The three gases will be stored outside and transported to the mixing station through heated metal tubing. The three gases flow continuously through the mixer, passing through a filter, relief valve, pneumatic shut-off valve, regulator, and flow controller. The flow controller settings determine the mixed gas composition. A separate flow meter monitors the resulting flow rate for each gas.

8.5.3 Distribution

The mixed gas will be transported between the mixing station and the detector through a one-inch diameter metal tubing. Supply manifolds on the detector will distribute the gas in parallel to 14 separate groups of chambers (six barrel sextants plus four quadrants on each endcap). Within each group, chambers in a given layer will be connected in series, while the different layers will be connected in parallel. Matching return manifolds will collect the gas for venting at a remote location. A blower will be used to reduce chamber over-pressure due to the back pressure of the vent line.

8.6 Front-End Electronics and High Voltage

The front-end electronics for the IFR will be located directly in the iron gaps of the flux return as close as possible to the detectors; the relatively high number of channels foreseen (∼40,000) requires that a certain amount of on-board processing be done in order to minimize the size of the outgoing cable plant. The electronic requirements for the detector are quite easy to fulfill—no pulse height data acquisition is foreseen. A single bit per struck strip has to be recorded and sent to the data acquisition system. The excellent timing properties of RPCs could also be exploited, and given the very low occupancy this subsystem is expected to have, a relatively small number of TDCs (one per layer) would be sufficient. The front-end electronics boards will include a very simple discriminator. The pulses originating from the RPC are quite large (200 mV) and do not have a large amplitude jitter, so a single transistor would be enough to standardize them and convert to TTL levels. Connection of the strips to the boards will use twisted and flat cables, at least one set of strips (either longitudinal or transverse) will be connected to the electronics through a very short cable path so that minimal deterioration of the timing characteristics will occur. High voltage will be individually fed to each detector (a typical configuration in the barrel will include between four and eight detectors per plane) through series resistors ($\sim$20 MΩ); small additional series resistors will be used as fuses so malfunctioning modules can be remotely disconnected from the HV supplies. Provision will be made for measuring and recording individual currents drawn from the detectors.

8.7 Final Assembly, Installation, and Monitoring

The major components of the IFR detectors (the Bakelite modules, readout strips, and the front-end electronics boards) will be manufactured at various institutions and shipped to SLAC for final assembly. Approximately 750 Bakelite modules each for the barrel and the endcaps will be manufactured in the RPC production plant in Italy. As they are manufactured, the modules will be shipped to Naples, Genoa, and Frascati for acceptance testing with cosmic ray muons with the accepted modules shipped to SLAC. The shipments will be staggered over an 18-month period with approximately 140 modules being shipped every three months. At SLAC, the modules will be processed in batches of $\sim$12 per week. Each module will be outfitted with a single, wide (20 cm) readout strip and inserted into a 12-chamber cosmic ray tower where they will be tested for high voltage plateau and gas integrity for approximately one day. After tests, the readout strip will be removed, and the modules corresponding to a given IFR layer will be placed side by side on a pallet, then joined at the seams with plastic film to form a single IFR detector plane. Full-length readout strips will be laminated across the modules of the detector plane. The front-end electronics cards will be mounted on the edge of the detector, which will be accessible from the open end of the barrel. For ϕ planes, the 4 m-long ϕ readout strips will be directly soldered to the front-end electronics cards added to the ends. On the z planes, the z strips terminate at the edge of the detector plane that is buried inside the IFR, so ribbon cable will be attached to the ends of the strips and folded at right angles to bring the signals out to the front-end electronics cards. The completed detector plane, on its pallet, will be inserted into a cosmic ray tower for detailed tests of the efficiency of each channel, using components of the *BaBar* data acquisition system. After final testing, the completed detector plane will be transported to the IR on its pallet. Each plane will be hoisted into position and slid off the pallet into the appropriate gap between the IFR plates. Spacers, wedged into the gap, will prevent the detectors from sliding within the gap. During operation, the efficiency of the IFR detector planes will be monitored by reconstructing muon pairs.

References

[Accel] A. Antonelli *et al.* (FENICE Collaboration), *Nucl. Instr. Methods* **A337**, 34 (1993);
E. Petrolo *et al.* (WA 92 Collaboration), *Nucl. Instr. Methods* **A315**, 45 (1992);
L. Antonazzi *et al.* (E 771 Collaboration), *Nucl. Instr. Methods* **A315**, 92 (1992);
C. Bacci *et al.* (RD 5 Collaboration), *Nucl. Instr. Methods* **A315**, 102 (1992).

[Bal94] R. Baldini-Ferroli, R. de Sangro, A. Palano, A. Zallo, "π/μ Discrimination with the Instrumented Flux Return," *BaBar Note* # 198 (1994).

[Calc94] A. Calcaterra, *BaBar Note* # 144 (1994).

[Cosmi] F. D'Aquino *et al.* (MINI Collaboration), *Nucl. Instr. Methods* **A324**, 330 (1993).
M. Ambrosio *et al.* (Cover Plastex Collaboration), *Nucl. Instr. Methods* **A344**, 350 (1994).

[Jaf94] D.E. Jaffe *et al.,* "Treatment of Weighted Events in a Likelihood Analysis of B_s oscillations or *CP* Violations," *BaBar Note* # 132 (1994).

[Lis94] L. Lista and S. Mele, "Study of Iron Segmentation Optimization of the I.F.R. Detector for $\pi\mu$ separation," *BaBar Note* # 194 (1994).

[LHC94] ATLAS Collaboration, *Nucl. Instr. Methods* **A340**, 466 (1994);
CMS Collaboration, *Nucl. Instr. Methods* **A334**, 98 (1994).

[L3RPC] A. Aloisio *et al.,* Proceedings of the Sixth Pisa Meeting on Advanced Detectors, Isola d'Elba, Italy (1994); submitted to *Nucl. Instr. Methods.*

[Plant] General Tecnica, Colli (FR) Italy.

[Pia94] M.G. Pia, "B Tagging with Muons," *BaBar Note* # 192 (1994).

[PDG94] L. Montanet *et al.* (Particle Data Group), *Phys. Rev.* **D50** (1994).

[San81] R. Santonico and R. Cardarelli, *Nucl. Instr. Methods* **A187**, 377 (1981).

[San88] R. Santonico and R. Cardarelli, *Nucl. Instr. Methods* **A263**, 20 (1988).

[Say68] G.A. Sayer and E.F. Beall, *Phys. Rev.* **169**, 1045 (1968).

[Wri94] D.M. Wright, "BEGET: The B-Factory Event Generator Version 21," *BaBar Note* # 149 (1994).

[Wri94b] D.M. Wright, "K_L^0 identification in $B^0 \to J/\psi\, K_L^0$ Decays," *BaBar Note* # 201 (1994).